Input Impedance Modeling and Verification of Single-Phase Voltage Source Converters Based on Harmonic Linearization

Han Zhang, *Student Member, IEEE*, Zhigang Liu, *Senior Member, IEEE*,
Siqi Wu, *Student Member, IEEE*, and Zhiyuan Li

***Abstract*—The impedance-based stability analysis of single-phase voltage source converters (VSCs) emphasizes the precise impedance modeling. Considering the complexity of dq-frame impedance modeling and measurement, this paper proposes a mirror-frequency impedance modeling and measurement approach of single-phase VSCs in the stationary frame based on harmonic linearization. First, the mirror frequency definition is put forward and the dynamics of the second-order generalized phase-locked loop considering the mirror-frequency effects is validated by simulations. Next, the impedance model considering the mirror-frequency effects and dc-link voltage control loops is compared with the conventional one-dimension impedance model and a mirror-frequency impedance measurement method is presented, which are verified by experiments on the hardware-in-the-loop platform. The results indicate that the mirror-frequency impedance model considering the dc-link voltage control is more accurate and better captures the cross-coupling dynamics of VSCs. Finally, the different bandwidths of dc-link voltage control loops and different capacitances are designed to study the impacts of dc-link voltage control loops and ripples on impedance. The experiments and impedance-based analysis illustrate that the wider bandwidth of dc-link voltage control loops or the less capacitance with high dc-link voltage ripple will expand the frequency range of negative impedance in the low frequency.**

***Index Terms*—Bandwidth, dc-link voltage control, dc voltage ripple, impedance model, mirror frequency, single-phase source voltage converter.**

I. Introduction

A LARGE number of voltage source converters (VSCs) have been utilized in distributed generation, HVDC transmission, railway traction drive systems, etc. The interactions between numerous converters and power systems may cause some unstable phenomena including harmonic instability, harmonic

---

Manuscript received July 22, 2018; revised September 30, 2018; accepted November 20, 2018. Date of publication November 26, 2018; date of current version June 10, 2019. This work was supported in part by the National Nature Science Foundation under Grants U1434203 and U1734202 and in part by the Sichuan Province Youth Science and Technology Innovation Team under Grant 2016TD0012. Recommended for publication by Associate Editor M. Ordonez. *(Corresponding author: Zhigang Liu.)*

The authors are with the School of Electrical Engineering, Southwest Jiaotong University, Chengdu 611756, China (e-mail:

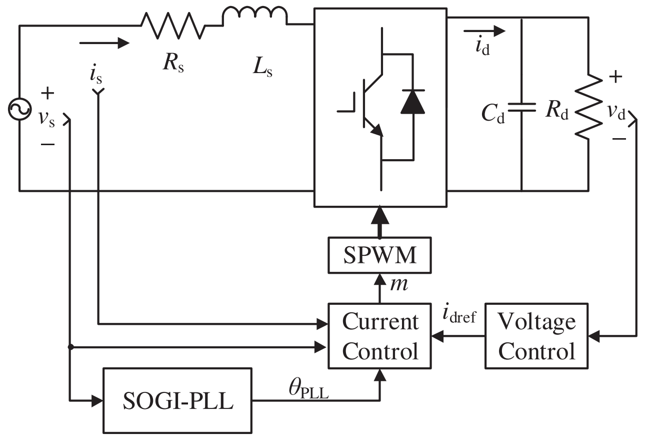

Fig. 1. Single-phase converter with the SOGI-PLL and the voltage and current control.

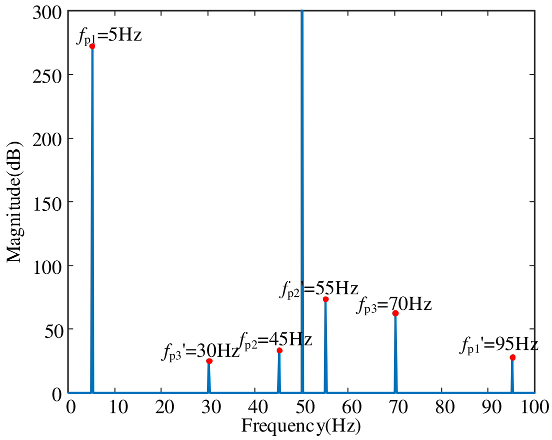

Fig. 2. FFT spectrum of ac currents.

two models are established in three-phase systems. There is no sequence impedance in single-phase VSCs. Therefore, Shah and Parsa established a two-dimension admittance model of single-phase VSCs, capturing the cross-coupling dynamics but neglecting the input voltage ripple components [18]. For single-phase VSCs, which are highly dq asymmetry, there is no effective impedance modeling and measurement method in the phase domain. The dc-link voltage control and the different bandwidths of voltage control loops of three-phase VSCs are analyzed in dq-domain, which proves that the dc-link voltage control loops and their bandwidths are critical for impedance-based stability analysis [19]. Consequently, for accurate impedance modeling of single-phase VSCs, it is necessary to consider the impacts of the dc-link voltage control loop and ripple on impedance.

The impedance model in [6], neglecting the dc-link voltage control, may lose some accuracy in impedance-based stability analysis. In this paper, the single-phase VSC of China Railway High-speed 3 (CRH3) electric multiple units (EMUs) with the voltage and current control is taken for instance, and a mirror-frequency impedance modeling and measurement method of single-phase VSCs based on harmonic linearization is developed. The rest of this paper is organized as follows. Section II describes the single-phase VSC and define the concept of the mirror frequency. Section III gives the impedance response of the second-order generalized integrator-PLL (SOGI-PLL) at mirror frequencies and establishes a conventional SISO impedance model and a mirror-frequency impedance model considering the dc-link voltage control, respectively. Section IV introduces an input mirror-frequency impedance measurement method. Experiments are made on the hardware-in-the-loop (HIL) simulation platform to verify the proposed impedance model, and the errors are discussed. Section V analyzes the effects of the different voltage control loop bandwidths and different dc-link voltage ripples on impedance response. Section VI concludes this paper.

II. MIRROR FREQUENCY DEFINITION

Fig. 1 shows a schematic diagram of a single-phase VSC with the SOGI-PLL and the voltage and the current control. The phase voltage is denoted as v_s, while the phase current is denoted as i_s. R_s and L_s denote the equivalent resistance and inductance of the traction transformer, respectively. R_d denotes the load and C_d denotes the dc-link capacitor. v_d denotes the output voltage. θ_{PLL} denotes the phase derived by the SOGI-PLL. m denotes the output modulation signal of the current control loop.

To establish a small-signal model or measure the ac-side impedance of the system, a small-signal voltage or current perturbation is usually injected into the ac system [8], [20]–[22]. Based on the simulation results, it is found that after a voltage perturbation $v_{pt} = V_{pt}\cos(2\pi f_p t)$ is injected into the ac side of the single-phase VSC, the ac current always generates the components at frequency f_p and $2f_1 - f_p$, where f_1 is the fundamental frequency. In this paper, the voltage source perturbations at frequency $f_{p1} = 5$ Hz, $f_{p2} = 45$ Hz, and $f_{p3} = 70$ Hz are injected, respectively. The fast Fourier transformation (FFT) spectrum analysis of the ac currents is drawn as Fig. 2.

In Fig. 2, the ac current components at frequencies f'_{p1}, f'_{p2}, and f'_{p3} are newly generated and correspond to the current components at f_{p1}, f_{p2}, and f_{p3}, respectively. The frequencies of the currents, newly produced, are equal to 95, 55, and 30 Hz and consistent with the theoretical results. Therefore, when the injected signal frequency is $f_p + f_1$, the corresponding signal frequency is $f_p - f_1$. The signals at frequency $f_p + f_1$ and $f_p - f_1$ are mirror-frequency signals and symmetric about the fundamental frequency f_1 in single-phase VSCs. The phenomenon has been explained in [18] and [22]. For clarity, in this paper, the signals at frequency $f_p + f_1$ are called as "positive-mirror-frequency" signals and the signals at frequency $f_p - f_1$ are called as "negative-mirror-frequency" signals. The subscript "p" denotes the "positive-mirror-frequency" signals and the subscript "n" denotes the "negative-mirror-frequency" signals. The reasons for appearance of mirror frequencies are caused by the convolution of the dc-link voltage ripple and the modulation signal, which will be explained later.

III. CLOSED-LOOP IMPEDANCE MODELING

A. Signal Definition

To establish a small-signal model of the VSC, a small voltage perturbation is usually injected into the ac side. In this paper, a small-signal voltage perturbation $v_p = V_p\cos[2\pi(f_p + f_1)t +$

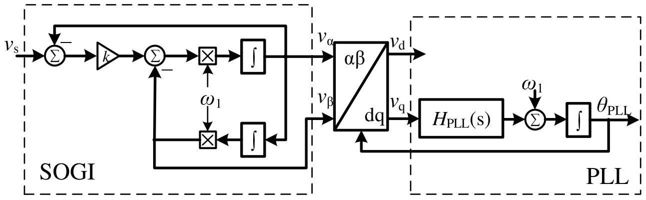

Fig. 3. Diagram of the SOGI-PLL.

$\theta_{vp}]$ is injected into the ac side of the single-phase VSC. Based on Section II, the mirror frequency of $f_p + f_1$ is $f_p - f_1$. Therefore, in the time domain, the phase voltage v_s and current i_s, considering the mirror frequency, are written as

$$\begin{aligned} v_s &= V_1 \cos(2\pi f_1 t + \theta_{v1}) + V_p \cos[2\pi(f_p + f_1)t + \theta_{vp}] \\ &\quad + V_n \cos[2\pi(f_p - f_1)t + \theta_{vn}] \end{aligned} \tag{1}$$

$$\begin{aligned} i_s &= I_1 \cos(2\pi f_1 t + \theta_{i1}) + I_p \cos[2\pi(f_p + f_1)t + \theta_{ip}] \\ &\quad + I_n \cos[2\pi(f_p + f_1)t + \theta_{\rm in}] \end{aligned} \tag{2}$$

where V_1 with θ_{v1} corresponds to the magnitude and phase of the fundamental voltage at frequency $f_1 .V_p$ with θ_{vp} corresponds to the magnitude and phase of the positive-mirror-frequency voltage perturbation at frequency $f_p + f_1 .V_n$ with θ_{vn} corresponds to the magnitude and phase of the negative-mirror-frequency voltage perturbation at frequency $f_p - f_1$. The current definition follows the same notation.

Considering the output dc-link voltage ripple, in the time domain, the dc voltage is written as

$$v_d = V_d + V_{dp} \cos(2\pi f_p t + \theta_{dp}) \tag{3}$$

where V_d corresponds to the magnitude of the dc-link voltage at frequency 0 Hz. V_{dp} with θ_{dp} corresponds to the magnitude and phase of the dc-link voltage ripple at frequency f_p.

Based on harmonic linearization, (1)–(3) can be written as frequency-domain equations

$$V_s[f] = \begin{cases} \dot{V}_1, f = \pm f_1 \\ \dot{V}_p, f = \pm(f_p + f_1) \\ \dot{V}_n, f = \pm(f_p - f_1) \end{cases} \tag{4}$$

$$I_s[f] = \begin{cases} \dot{I}_1, f = \pm f_1 \\ \dot{I}_p, f = \pm(f_p + f_1) \\ \dot{I}_n, f = \pm(f_p - f_1) \end{cases} \tag{5}$$

$$V_d[f] = \begin{cases} V_d, f = 0 \\ \dot{V}_{dp}, f = \pm f_p \end{cases} \tag{6}$$

where $\dot{V}_1 = (V_1/2)e^{\pm j\theta_{v1}}$, $\dot{V}_p = (V_p/2)e^{\pm j\theta_{vp}}$, $\dot{V}_n = (V_n/2)e^{\pm j\theta_{vn}}$, and others follow the same notation [3], [18].

B. SOGI-PLL Modeling

Fig. 3 shows the diagram of the SOGI-PLL to track the phase of the phase voltage v_s [8], [10], [18], [23]. The voltage v_α is aligned with the phase voltage v_s. The voltage v_β, lagging v_α 90°, is generated by the SOGI. $\omega 1 = 2\pi f_1$ is the fundamental angular frequency. Due to the voltage perturbation in v_s, in the time domain, voltage v_α and v_β can be written as

$$\begin{aligned} v_\alpha &= V_1 \cos(2\pi f_1 t + \theta_{v1}) + V_{\alpha p} \cos[2\pi(f_p + f_1)t + \theta_{\alpha p}] \\ &\quad + V_{\alpha n} \cos[2\pi(f_p - f_1)t + \theta_{\alpha n}] \end{aligned} \tag{7}$$

$$\begin{aligned} v_\beta &= V_1 \sin(2\pi f_1 t + \theta_{v1}) + V_{\beta p} \cos[2\pi(f_p + f_1)t + \theta_{\beta p}] \\ &\quad + V_{\beta n} \cos[2\pi(f_p - f_1)t + \theta_{\beta n}]. \end{aligned} \tag{8}$$

The transfer functions from v_α and v_β to v_s are deduced as

$$H_\alpha(s) = \frac{V_\alpha(s)}{V_s(s)} = \frac{k\omega_1 s}{s^2 + k\omega_1 s + \omega_1^2} \tag{9}$$

$$H_\beta(s) = \frac{V_\beta(s)}{V_s(s)} = \frac{k\omega_1^2}{s^2 + k\omega_1 s + \omega_1^2}. \tag{10}$$

Substituting (9) and (10) into (7) and (8), the frequency-domain expressions of v_α and v_β are

$$V_\alpha[f] = \begin{cases} \dot{V}_1, f = \pm f_1 \\ \dot{V}_{\alpha p} = \dot{V}_p H_\alpha(s + j\omega_1), f = \pm(f_p + f_1) \\ \dot{V}_{\alpha n} = \dot{V}_n H_\alpha(s - j\omega_1), f = \pm(f_p - f_1) \end{cases} \tag{11}$$

$$V_\beta[f] = \begin{cases} \mp j\dot{V}_1, f = \pm f_1 \\ \dot{V}_{\beta p} = \dot{V}_p H_\beta(s + j\omega_1), f = \pm(f_p + f_1) \\ \dot{V}_{\beta n} = \dot{V}_n H_\beta(s - j\omega_1), f = \pm(f_p - f_1). \end{cases} \tag{12}$$

Since the single-phase system is unbalanced in the phase domain, there exists a phase deviation $\Delta\theta = \theta_{\rm PLL} - \theta_1$, for solving the nonlinearity in Park's transformation, the Park's transformation from $\alpha\beta$-frame to dq-frame can be divided into two parts as

$$\begin{aligned} T_{dq/\alpha\beta}(\theta_{\rm PLL}) &= \begin{bmatrix} \cos(\theta_{\rm PLL} - 90^\circ) & \sin(\theta_{\rm PLL} - 90^\circ) \\ -\sin(\theta_{\rm PLL} - 90^\circ) & \cos(\theta_{\rm PLL} - 90^\circ) \end{bmatrix} \\ &= \begin{bmatrix} \cos(\theta_1 - 90^\circ) & \sin(\theta_1 - 90^\circ) \\ -\sin(\theta_1 - 90^\circ) & \cos(\theta_1 - 90^\circ) \end{bmatrix} \\ &\quad \times \begin{bmatrix} \cos\Delta\theta & \sin\Delta\theta \\ -\sin\Delta\theta & \cos\Delta\theta \end{bmatrix} \end{aligned} \tag{13}$$

where $\theta_1 = 2\pi f_1 t$ is the phase of the phase voltage v_s, which neglects the influence of the PLL dynamics. And -90° ensures the d-frame component be equal to the amplitude of the ac quantity [8]. Without considering the PLL dynamics, the output voltage in the dq-frame is solved as

$$\begin{bmatrix} v_{du} \\ v_{qu} \end{bmatrix} = \begin{bmatrix} \cos(\theta_1 - 90^\circ) & \sin(\theta_1 - 90^\circ) \\ -\sin(\theta_1 - 90^\circ) & \cos(\theta_1 - 90^\circ) \end{bmatrix} \begin{bmatrix} v_\alpha \\ v_\beta \end{bmatrix} \tag{14}$$

where the subscript "*u*" denotes the voltage-frame variables. Substituting (7) and (8) into (14) yields

$$\begin{aligned} v_{qu} = {} & V_1 \cos\theta_{v1} \\ & + \frac{V_{\alpha p}}{2}[\cos(2\pi f_p t + 2\pi f_1 t + \theta_{\alpha p}) + \cos(2\pi f_p t + \theta_{\alpha p})] \\ & + \frac{V_{\alpha n}}{2}[\cos(2\pi f_p t + \theta_{\alpha n}) + \cos(2\pi f_p t - 2\pi f_1 t + \theta_{\alpha n})] \\ & + \frac{V_{\beta p}}{2}[\sin(2\pi f_p t + 2\pi f_1 t + \theta_{\beta p}) - \sin(2\pi f_p t + \theta_{\beta p})] \\ & + \frac{V_{\beta n}}{2}[-\sin(2\pi f_p t - 2\pi f_1 t + \theta_{\beta n}) + \sin(2\pi f_p t + \theta_{\beta n})]. \end{aligned} \tag{15}$$

Different from [18], the second-order harmonic elements at frequency $f_p \pm 2f_1$ are considered in (15) for more precise modeling. And through the Fourier transform, it is rewritten as

$$V_{qv}[f] = \begin{cases} V_1 \cos\theta_{v1}, f = 0 \\ \dfrac{\dot{V}_{\alpha p} + \dot{V}_{\alpha n} \pm j\dot{V}_{\beta p} \mp j\dot{V}_{\beta n}}{2}, f = \pm f_p \\ \dfrac{\dot{V}_{\alpha p} \mp j\dot{V}_{\beta p}}{2}, f = \pm(f_p + 2f_1) \\ \dfrac{\dot{V}_{\alpha n} \pm j\dot{V}_{\beta n}}{2}, f = \pm(f_p - 2f_1). \end{cases} \tag{16}$$

The linear response of $\Delta\theta$ is given by [3], [18], and [23]

$$\Delta\theta = T_{\mathrm{PLL}}(s) \cdot V_{qu}(s) \tag{17}$$

where $T_{\mathrm{PLL}}(s) = \frac{H_{\mathrm{PLL}}(s)/s}{1+V_1 \cdot H_{\mathrm{PLL}}(s)/s}$ and $H_{\mathrm{PLL}}(s)$ is a loop compensator.

The frequency-domain expression of $\cos(\theta_{\mathrm{PLL}})$ and $\sin(\theta_{\mathrm{PLL}})$ are listed as follows:

$$\cos(\theta_{\mathrm{PLL}})[f] = \begin{cases} \frac{1}{2} \pm \frac{1}{2} j \cos\theta_{v1}, f = \pm f_1 \\ \pm\frac{1}{4} jT_{\mathrm{PLL}}(s)(\dot{V}_{\alpha p} + \dot{V}_{\alpha n} \pm j\dot{V}_{\beta p} \mp j\dot{V}_{\beta n}) \\ \mp\frac{1}{4} jT_{\mathrm{PLL}}(s \pm j4\pi f_1)(\dot{V}_{\alpha p} \mp j\dot{V}_{\beta p}), f = \pm(f_p + f_1) \\ \mp\frac{1}{4} jT_{\mathrm{PLL}}(s)(\dot{V}_{\alpha p} + \dot{V}_{\alpha n} \pm j\dot{V}_{\beta p} \mp j\dot{V}_{\beta n}) \\ \pm\frac{1}{4} jT_{\mathrm{PLL}}(s \mp j4\pi f_1)(\dot{V}_{\alpha n} \pm j\dot{V}_{\beta n}), f = \pm(f_p - f_1) \end{cases} \tag{18}$$

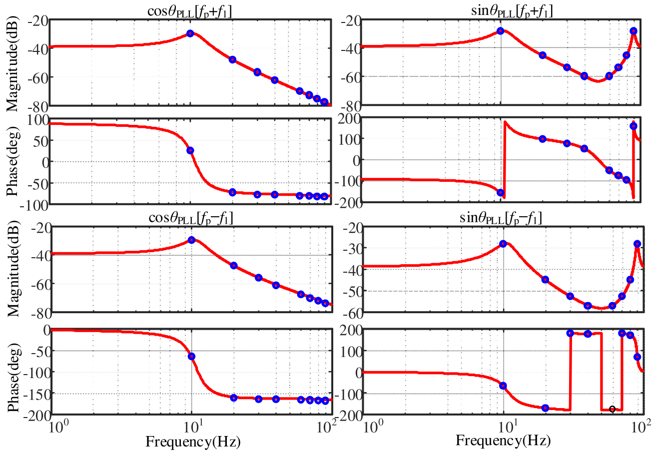

Fig. 4. Modeled and measured response of $\cos\theta_{\mathrm{PLL}}$ and $\sin\theta_{\mathrm{PLL}}$.

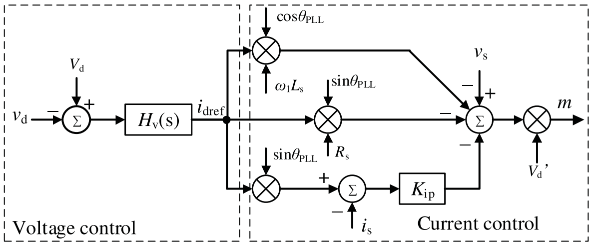

Fig. 5. Block diagram of the voltage and current control.

$$\sin\theta_{\mathrm{PLL}}[f] = \begin{cases} \mp\frac{1}{2} j + \frac{1}{2}\cos\theta_{v1}, f = \pm f_1 \\ \frac{1}{4} T_{\mathrm{PLL}}(s)(\dot{V}_{\alpha p} + \dot{V}_{\alpha n} \pm j\dot{V}_{\beta p} \mp j\dot{V}_{\beta n}) \\ \quad + \frac{1}{4} T_{\mathrm{PLL}}(s \pm j4\pi f_1)(\dot{V}_{\alpha p} \mp j\dot{V}_{\beta p}), f = \pm(f_p + f_1) \\ \frac{1}{4} T_{\mathrm{PLL}}(s)(\dot{V}_{\alpha p} + \dot{V}_{\alpha n} \pm j\dot{V}_{\beta p} \mp j\dot{V}_{\beta n}) \\ \quad + \frac{1}{4} T_{\mathrm{PLL}}(s \mp j4\pi f_1)(\dot{V}_{\alpha n} \pm j\dot{V}_{\beta n}), f = \pm(f_p - f_1). \end{cases} \tag{19}$$

To validate the response of $\cos\theta_{\mathrm{PLL}}$ and $\sin\theta_{\mathrm{PLL}}$ in the frequency domain in (18) and (19), the modeled and measured response of $\cos\theta_{\mathrm{PLL}}$ and $\sin\theta_{\mathrm{PLL}}$ at frequency $f_p \pm f_1$ are plotted on four sub-Bode diagrams in Fig. 4. The red lines and the blue circles denote the modeled and measured response of $\cos\theta_{\mathrm{PLL}}$ and $\sin\theta_{\mathrm{PLL}}$, respectively. The results show that the measured response matches well with the modeled response. Therefore, the modeling approach of $\cos\theta_{\mathrm{PLL}}$ and $\sin\theta_{\mathrm{PLL}}$ at the positive and negative-mirror frequency is precise.

C. Voltage Control and Current Control

The single-phase converter of CRH3 EMUs utilizes the voltage and current control, which is illustrated in Fig. 5. The current control adopts the proportional controller. The voltage control uses the proportional–integral (PI) controller, which ensures the constant dc-link voltage. But there is a small dc-link voltage ripple, the frequency-domain expression of the output of the dc-link voltage control loop i_{dref} is

$$I_{\mathrm{dref}}[f] = \begin{cases} I_{\mathrm{ref}},\ f = 0 \\ -V_d[f]H_v[f],\ f = \pm f_p \end{cases} \tag{20}$$

where I_{ref} is the reference for the input current. $H_v = K_{vp} + K_{vi}/s$ is the transfer function of the voltage control loop.

First, from the block diagram in Fig. 5, the time-domain expression of the output of the current control loop m can be written as

$$\begin{aligned} m = V'_d\{&v_s - i_{\mathrm{dref}} \cdot \omega_1 L_s \cdot \cos\theta_{\mathrm{PLL}} - i_{\mathrm{dref}} \cdot R_s \cdot \sin\theta_{\mathrm{PLL}} \\ &- K_{ip} \cdot i_{\mathrm{dref}} \cdot \sin\theta_{\mathrm{PLL}} + K_{ip} \cdot i_s\}. \end{aligned} \tag{21}$$

By Fourier transform, in the frequency domain, (21) is rewritten as (22) as shown at the bottom of this page.

D. Closed-Loop Impedance Modeling

First, as the circuit topology depicted in Fig. 1, the time-domain circuit equation can be written as

$$\begin{cases} v_s - \left(R_s \cdot i_s + L_s \dfrac{di_s}{dt}\right) = m \cdot v_d \\ m \cdot i_s = \dfrac{v_d}{R_d} + C_d \dfrac{dv_d}{dt}. \end{cases} \tag{23}$$

Then, based on harmonic linearization [20], [24], at frequency f, the frequency-domain expression of (23) can be written as

$$V_s[f] - (R_s + j2\pi f L_s)I_s[f] = M[f] \otimes V_d[f] \tag{24}$$

$$M[f] \otimes I_s[f] = (1/R_d + j2\pi f C_d)V_d[f] \tag{25}$$

where "⊗" denotes the convolution symbol.

In Case 1, the dc-link voltage ripple and the mirror-frequency coupling effects are neglected. Equation (22) is rewritten as

$$\begin{aligned} &M_{\mathrm{case1}}[f] \\ &= \begin{cases} V'_d\{V_s[f] + K_{ip}I_s[f] + \omega_1 L_s I_{\mathrm{ref}} \cos\theta_{\mathrm{PLL}}[f] \\ \quad + (R_s + K_{ip})I_{\mathrm{ref}} \sin\theta_{\mathrm{PLL}}[f]\},\ f = \pm f_1 \\ V'_d\{V_s[f] + K_{ip}I_s[f] - \omega_1 L_s(I_{\mathrm{ref}} \cos\theta_{\mathrm{PLL}}[f]) \\ \quad - (R_s + K_{ip})(I_{\mathrm{ref}} \sin\theta_{\mathrm{PLL}}[f]\},\ f = \pm(f_p + f_1) \\ V'_d\{V_s[f] + K_{ip}I_s[f] - \omega_1 L_s(I_{\mathrm{ref}} \cos\theta_{\mathrm{PLL}}[f]) \\ \quad - (R_s + K_{ip})(I_{\mathrm{ref}} \sin\theta_{\mathrm{PLL}}[f]\},\ f = \pm(f_p - f_1). \end{cases} \end{aligned} \tag{26}$$

Substituting (26) into (24), at the positive-mirror frequency $f_p + f_1$, (24) is rewritten as

$$\begin{aligned} &\dot{V}_p^+ - [R_s + j2\pi(f_p + f_1)L_s]\dot{I}_p^+ = M_{\mathrm{case1}}[f_p + f_1]V_d \\ &= V'_d V_d\{\dot{V}_p^+ + K_{ip}\dot{I}_p^+ - \omega_1 L_s I_{\mathrm{ref}} \cos[f_p + f_1] \\ &\quad - (R_s + K_{ip})I_{\mathrm{ref}} \sin[f_p + f_1]\} \end{aligned} \tag{27}$$

where the superscripts "+" and "−" mean that each frequency-domain variable is derived at the positive and negative frequencies. For instance, $\dot{V}_p^+ = (V_p/2)e^{+j\theta_{vp}}$, $f = +(f_p + f_1)$, $\dot{V}_p^- = (V_p/2)e^{-j\theta_{vp}}$, and $f = -(f_p + f_1)$.

Substituting (18) and (19) into (27), the positive-mirror-frequency impedance $\mathrm{Z}_{ppcase1}$ can be deduced as

$$\begin{aligned} Z_{pp1} = \frac{\dot{V}_p^+}{\dot{I}_p^+} = &[R_s + j2\pi(f_p + f_1)L_s + V'_d V_d K_{ip}]/ \\ &\left\{1 - V'_d V_d + V'_d V_d \omega_1 L_s I_{\mathrm{ref}} \frac{1}{4} j(T_{\mathrm{PLL}}(s)[H_\alpha(s + j\omega_1)\right. \\ &+ jH_\beta(s + j\omega_1)] - T_{\mathrm{PLL}}(s + j4\pi f_1)[H_\alpha(s + j\omega_1) \\ &- jH_\beta(s + j\omega_1)]) + V'_d V_d(R_s + K_{ip})I_{\mathrm{ref}} \frac{1}{4} \\ &\times (T_{\mathrm{PLL}}(s)[H_\alpha(s + j\omega_1) + jH_\beta(s + j\omega_1)] \\ &\left. + T_{\mathrm{PLL}}(s + j4\pi f_1)[H_\alpha(s + j\omega_1) - jH_\beta(s + j\omega_1)])\right\}. \end{aligned} \tag{28}$$

At the negative-mirror frequency $f_p - f_1$, (24) is rewritten as

$$\begin{aligned} &\dot{V}_n^+ - [R_s + j2\pi(f_p - f_1)L_s]\dot{I}_n^+ = M_{\mathrm{case1}}[f_p - f_1]V_d \\ &= V'_d V_d\{\dot{V}_n^+ + K_{ip}\dot{I}_n^+ - \omega_1 L_s I_{\mathrm{ref}} \cos[f_p - f_1] \\ &\quad - (R_s + K_{ip})I_{\mathrm{ref}} \sin[f_p - f_1]\}. \end{aligned} \tag{29}$$

Substituting (18) and (19) into (29), the negative-mirror-frequency impedance $\mathrm{Z}_{nncase1}$ can be deduced as

$$\begin{aligned} Z_{nn1} = \frac{\dot{V}_n^+}{\dot{I}_n^+} = &[R_s + j2\pi(f_p - f_1)L_s + V'_d V_d K_{ip}]/ \\ &\left\{1 - V'_d V_d - V'_d V_d \omega_1 L_s I_{\mathrm{ref}} \frac{1}{4} j(T_{\mathrm{PLL}}(s)[H_\alpha(s - j\omega_1)\right. \\ &- jH_\beta(s - j\omega_1)] - T_{\mathrm{PLL}}(s - j4\pi f_1)[H_\alpha(s - j\omega_1) \\ &+ jH_\beta(s - j\omega_1)]) + V'_d V_d(R_s + K_{ip})I_{\mathrm{ref}} \frac{1}{4} \\ &\times (T_{\mathrm{PLL}}(s)[H_\alpha(s - j\omega_1) - jH_\beta(s - j\omega_1)] \\ &\left. + T_{\mathrm{PLL}}(s - j4\pi f_1)[H_\alpha(s - j\omega_1) + jH_\beta(s - j\omega_1)])\right\}. \end{aligned} \tag{30}$$

$$M[f] = \begin{cases} V'_d\{V_s[f] + K_{ip}I_s[f] + \omega_1 L_s I_{\mathrm{ref}} \cos\theta_{\mathrm{PLL}}[f] + (R_s + K_{ip})I_{\mathrm{ref}} \sin\theta_{\mathrm{PLL}}[f]\},\ f = \pm f_1 \\ V'_d\{V_s[f] + K_{ip}I_s[f] - \omega_1 L_s(I_{\mathrm{ref}} \cos\theta_{\mathrm{PLL}}[f] + I_{\mathrm{dref}}[\pm f_p] \cos\theta_{\mathrm{PLL}}[\pm f_1]) \\ \quad -(R_s + K_{ip})(I_{\mathrm{ref}} \sin\theta_{\mathrm{PLL}}[f] + I_{\mathrm{dref}}[\pm f_p] \sin\theta_{\mathrm{PLL}}[\pm f_1])\},\ f = \pm(f_p + f_1) \\ V'_d\{V_s[f] + K_{ip}I_s[f] - \omega_1 L_s(I_{\mathrm{ref}} \cos\theta_{\mathrm{PLL}}[f] + I_{\mathrm{dref}}[\pm f_p] \cos\theta_{\mathrm{PLL}}[\mp f_1]) \\ \quad -(R_s + K_{ip})(I_{\mathrm{ref}} \sin\theta_{\mathrm{PLL}}[f] + I_{\mathrm{dref}}[\pm f_p] \sin\theta_{\mathrm{PLL}}[\mp f_1])\},\ f = \pm(f_p - f_1) \end{cases} \tag{22}$$

In Case 2, the dc-link voltage ripple and the mirror-frequency effects are both considered. Due to the complexity of the impedance calculation, the detailed deduction is omitted in this section and will be provided in the Appendix. The mirror-frequency impedance are listed as (31)–(34) as shown at the bottom of this page.

In Case 2, the mirror-frequency impedance $\boldsymbol{Z}_{pn2}$ is a second-order matrix, which includes the cross-coupling elements Z_{pn2} and Z_{np2}. In Case 1, the mirror-frequency impedance only contains two diagonal elements Z_{pp1} and Z_{nn1}. Without considering the mirror-frequency and the dc-link voltage ripple effects, the system is a SISO system. In contrast, considering the mirror-frequency and the dc-link voltage ripple effects, the system is a multiple input multiple output (MIMO) system. The cross-coupling impedance does not have a deep physical meaning but reflects the relationship between the positive and negative-mirror-frequency signals.

Actually, considering the high-order harmonic elements in single-phase VSCs at positive-mirror frequency, (24) can be rewritten as

$$\begin{aligned}\dot{V}_p^+ - [R_s + j2\pi(f_p + f_1)L_s]\dot{I}_p^+ \\ = M[f_p + hf_1]V_d[(1-h)f_1] + M[(1-h)f_1]V_d[f_p + hf_1]\end{aligned} \tag{35}$$

where "h" is an integer. In this paper, the second-order harmonic elements are overlooked and (35) is simplified as

$$\begin{aligned}\dot{V}_p^+ - [R_s + j2\pi(f_p + f_1)L_s]\dot{I}_p^+ = M[f_p + f_1]V_d[0] \\ + M[f_1]V_d[f_p].\end{aligned} \tag{36}$$

Although $V_d[f_p]$ is a small-signal variable compared with V_d, it should be considered in (25), which can be deduced as

$$\begin{aligned}I_s[f_p - f_1] = &\frac{(1/R_d + j2\pi f_p C_d)V_d[f_p]}{M[f_1]} - \frac{M[-f_1]I_s[f_p + f_1]}{M[f_1]} \\ &- \frac{M[f_p + f_1]I_s[-f_1]}{M[f_1]} - \frac{M[f_p - f_1]I_s[f_1]}{M[f_1]}\end{aligned} \tag{37}$$

where $I_s[f_p - f_1]$ is the mirror-frequency current of $I_s[f_p + f_1]$. Equation (37) gives the newly generated current $I_s[f_p - f_1]$ through the formula deduction. The signal flow can help us visually understand the flow of the small-signal perturbation through converters and frequency cross-coupling among different variables [18], [25]. The nodes represent the variables, and the lines represent the signal flow between any two variables. For example, in Fig. 6, it can be observed that, there is a path from the voltage $V_s(s + \mathrm{j}\omega_1)$ to the current $I_s(s + \mathrm{j}\omega_1)$. Besides, there is another path from the modulation signal $M(s \pm \mathrm{j}\omega_1)$ to the current $I_s(s + \mathrm{j}\omega_1)$, and there is a path from the dc voltage perturbation $V_d(s)$ to the modulation signal $M(s \pm \mathrm{j}\omega_1)$. Many frequency cross-couplings are generated in the single-phase VSC.

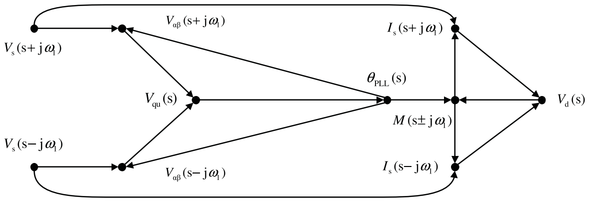

Fig. 6. Harmonic signal-flow graph of the VSC.

IV. IMPEDANCE MEASUREMENT AND VERIFICATION

A. Impedance Measurement Method

A perturbation injection approach based on frequency scanning is a popular method in impedance measurement [8], [14]. For one-dimension conventional impedance [18], [26], [27], the input impedance is the ratio of the perturbation voltage and the response current at the same frequency. For the decoupling sequence impedance has the same definition [15]. But for the mirror-frequency impedance, a voltage perturbation will produce two different response currents at mirror frequencies. Therefore, two independent voltage perturbations v_{pt1} and v_{pt2} should be injected into two same systems, respectively, as depicted in Fig. 7. The ac small-signal variables V_{s1}, V_{s2}, I_{s1}, and I_{s2} are derived by FFT for impedance calculation.

The expressions of the two independent voltage perturbations are written as

$$\begin{cases} v_{pt1} = V_p \cos[2\pi(f_p + f_1)t + \theta_{vp}] \\ v_{pt2} = V_n \cos[2\pi(f_p - f_1)t + \theta_{vn}]. \end{cases} \tag{38}$$

Referring to [8], [15], and [21], the two perturbations yield

$$\begin{pmatrix} \dot{V}_{p1}^+ \\ \dot{V}_{n1}^+ \end{pmatrix} = \begin{pmatrix} Z_{pp} & Z_{pn} \\ Z_{np} & Z_{nn} \end{pmatrix} \begin{pmatrix} \dot{I}_{p1}^+ \\ \dot{I}_{n1}^+ \end{pmatrix} \tag{39}$$

$$\begin{pmatrix} \dot{V}_{p2}^+ \\ \dot{V}_{n2}^+ \end{pmatrix} = \begin{pmatrix} Z_{pp} & Z_{pn} \\ Z_{np} & Z_{nn} \end{pmatrix} \begin{pmatrix} \dot{I}_{p2}^+ \\ \dot{I}_{n2}^+ \end{pmatrix}. \tag{40}$$

$$Z_{pp2} = \frac{R_s + j2\pi(f_p + f_1)L_s + V'_d V_d K_{ip} + (V_d B_1 + \dot{M}_1^+)/G(\dot{I}_1^- V'_d K_{ip} + \dot{M}_1^-)}{1 - V'_d V_d - V_d A_3 - (V_d B_1 + \dot{M}_1^+)/G(\dot{I}_1^- V'_d + \dot{I}_1^- A_3 + \dot{I}_1^+ A_5)} \tag{31}$$

$$Z_{pn2} = \frac{(V_d B_1 + \dot{M}_1^+)/G(\dot{I}_1^+ V'_d K_{ip} + \dot{M}_1^+)}{1 - V'_d V_d - V_d A_3 - (V_d B_1 + \dot{M}_1^+)/G(\dot{I}_1^- V'_d + \dot{I}_1^- A_3 + \dot{I}_1^+ A_5)} \tag{32}$$

$$Z_{np2} = \frac{(B_2 V_d + \dot{M}_1^-)/G(\dot{I}_1^- V'_d K_{ip} + \dot{M}_1^-)}{1 - V'_d V_d - V_d A_6 - (B_2 V_d + \dot{M}_1^-)/G(\dot{I}_1^+ V'_d + \dot{I}_1^- A_4 + \dot{I}_1^+ A_6)} \tag{33}$$

$$Z_{nn2} = \frac{R_s + j2\pi(f_p - f_1)L_s + V'_d V_d K_{ip} + (B_2 V_d + \dot{M}_1^-)/G(\dot{I}_1^+ V'_d K_{ip} + \dot{M}_1^+)}{1 - V'_d V_d - V_d A_6 - (B_2 V_d + \dot{M}_1^-)/G(\dot{I}_1^+ V'_d + \dot{I}_1^- A_4 + \dot{I}_1^+ A_6)} \tag{34}$$

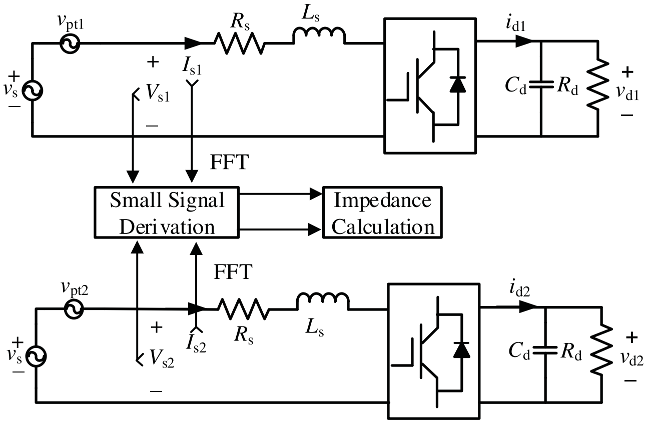

Fig. 7. Mirror-frequency impedance measurement method for single-phase converters.

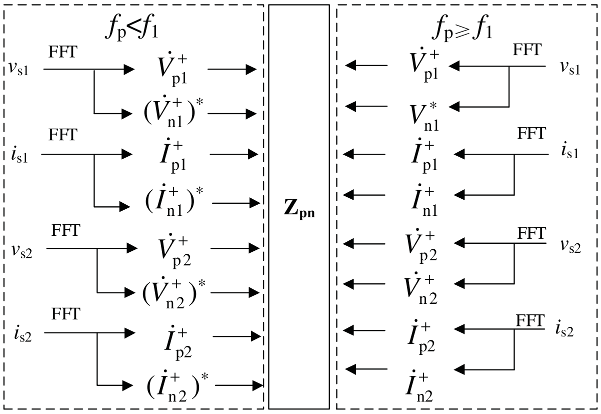

Fig. 8. Mirror-frequency impedance calculation procedure.

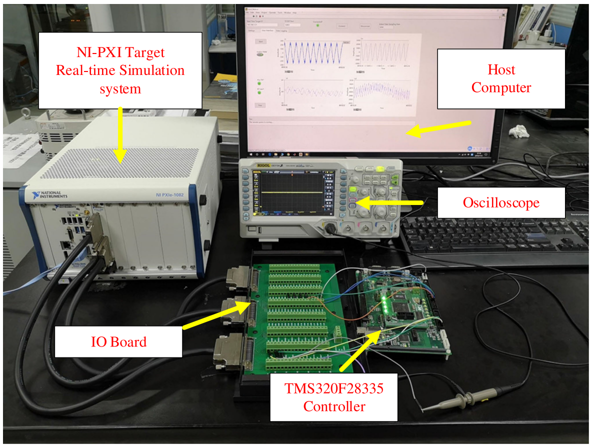

Fig. 9. HIL simulation platform.

TABLE I
PARAMETERS OF SINGLE-PHASE VSC

Number	Parameters	Value
1	Equivalent resistance R_s/Ω	0.145
2	Equivalent inductance L_s/mH	2.3
3	Fundamental frequency f_1/Hz	50
4	DC-link capacitance C_d/mF	3
5	Load R_d/Ω	50
6	Switching frequency f_{sw}/Hz	350
7	output constant voltage V_d/V	3000
8	Proportion gain of current controller K_{ip}	30
9	Proportion gain of SOGI k	1.414
10	Proportional gain of $H_{PLL}(s)$ K_{pPLL}	0.9848
11	Integral gain of $H_{PLL}(s)$ K_{iPLL}	1063.2
12	Proportional gain of voltage controller K_{vp}	0.01
13	Integral gain of voltage controller K_{vi}	10
14	Amplitude of voltage source V_1/V	2191.7
15	Sampling frequency f_{sa}/kHz	20

With the combination of (39) and (40), the mirror-frequency impedance calculation formula are listed as follows:

$$\begin{pmatrix} Z_{pp} & Z_{pn} \\ Z_{np} & Z_{nn} \end{pmatrix} = \begin{pmatrix} \dot{V}^+_{p1} & \dot{V}^+_{p2} \\ \dot{V}^+_{n1} & \dot{V}^+_{n2} \end{pmatrix} \begin{pmatrix} \dot{I}^+_{p1} & \dot{I}^+_{p2} \\ \dot{I}^+_{n1} & \dot{I}^+_{n2} \end{pmatrix}. \tag{41}$$

To make sure that (31) holds, $[\dot{V}^+_{p1}, \dot{V}^+_{n1}]^T$ and $[\dot{V}^+_{p2}, \dot{V}^+_{n2}]^T$ are linearly independent, $[\dot{I}^+_{p1}, \dot{I}^+_{n1}]^T$ and $[\dot{I}^+_{p2}, \dot{I}^+_{n2}]^T$, too [28]. Some signals are defined in the negative frequency domain in (4) and (5), etc. The negative frequency means that the frequency is lower than 0 Hz. However, there is no negative frequencies in the actual system. Thus, the frequency of voltage perturbation v_{pt2} is actually the absolute value of $f_p - f_1$. The impedance calculation formula should be discussed according to the size relationship between f_p and f_1. In (4), (5), and other formulas and definitions, it is found that the signals in opposite frequency are conjugate complex numbers. Therefore, this paper designs a mirror-frequency impedance calculation method, as depicted in Fig. 8.

In Fig. 8, time-domain variables are transformed into frequency-domain variables by FFT. The superscript "$*$" represents the conjugate operator. When $f_p < f_1$, the mirror-frequency impedance calculation follows the procedure in the left dotted-line frame. When $f_p \geq f_1$, the mirror-frequency impedance calculation follows the procedure in the right dotted-line frame. The final impedance calculation formula of $\boldsymbol{Z}_{pn}$, in the two conditions, adopts (41).

B. Impedance Verification

In order to verify the mirror-frequency impedance modeling, measurement and calculation approach proposed in this paper, experiments are performed correspondingly based on the HIL platform, as shown in Fig. 9. The model of the single-phase converter is developed in the electromagnetic transient simulation software StarSim and runs on NI-PXIe-FPGA-7868R based real-time HIL system with the time step of 1 μs [29]. The current and voltage controllers are implemented a TMS320F28335 DSP and the sampling frequency is set as 20 kHz. The green terminal board contains many IO channels, connecting the HIL simulation system to the controller DSP. The oscilloscope measures the output dc voltage of the single-phase converter. The graphical user interface of the host computer shows the ac and dc voltages and currents, and it can display all the relevant data and measurements of the system. Parameters for these experiments are provided in Table I.

The bandwidth of the PLL is set as 500 Hz, higher than the switching frequency. The magnitudes and phases of the modeled and measured impedance are plotted on four sub-Bode diagrams in Fig. 10. The blue lines denote the modeled impedance in

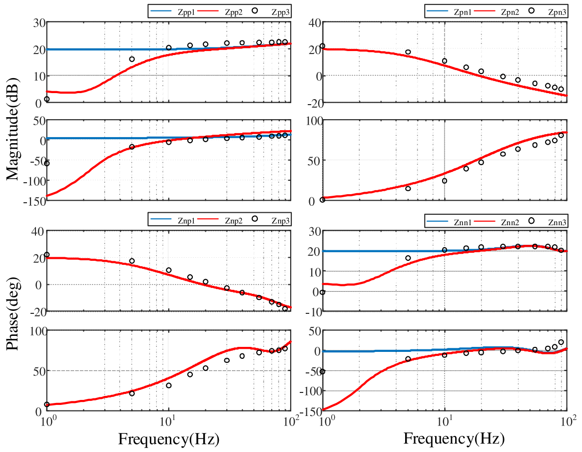

Fig. 10. Modeled and measured impedance in Cases 1 and 2.

TABLE II
PARAMETERS OF DC-LINK VOLTAGE CONTROLLERS

Number	Parameters	Value	Bandwidth
1	Proportional gain of voltage controller K_{vp1}	0.1	16 Hz
2	Proportional gain of voltage controller K_{vp2}	1	75 Hz
3	Proportional gain of voltage controller K_{vp3}	10	310 Hz
4	Proportional gain of voltage controller K_{vp4}	20	445 Hz
5	Integral gain of voltage controller K_{vi1}	10	16 Hz
6	Integral gain of voltage controller K_{vi2}	10	75 Hz
7	Integral gain of voltage controller K_{vi3}	10	310 Hz
8	Integral gain of voltage controller K_{vi4}	10	445 Hz

Case 1, including Z_{pp1} and Z_{nn1}. The red lines denote the modeled impedance in Case 2, including Z_{pp2}, Z_{pn2}, Z_{np2}, and Z_{nn2}. Eleven perturbation frequencies f_p among [1 Hz, 100 Hz] are selected to fulfill the impedance measurement. The black circles denote the measured impedance.

The results show that the measured impedance response is matched well with the mirror-frequency impedance in Case 2, which validates that the mirror-frequency impedance modeling approach is accurate. The impedance without considering the mirror-frequency effects and the dc-link voltage ripple do not match well with the measured impedance, which reveals that there are some errors among the impedance modeling without considering mirror-frequency effects. Besides, the measured impedance Z_{pn3} and Z_{np3} proves that the cross-coupling elements exist and should not be neglected. It can be observed that the dc-link voltage control loops and ripples result in the frequency cross-couplings in single-phase VSCs.

V. EFFECTS OF BANDWIDTH OF DC-LINK VOLTAGE CONTROL LOOP AND DC-LINK VOLTAGE RIPPLE ON IMPEDANCE

A. Effects of DC-Link Voltage Controls Loops with Different Bandwidths on Impedance Response

To investigate the impacts of the dc voltage control loops with different bandwidths, the mirror-frequency impedance model is analyzed with four sets of dc voltage controller parameters. The integral gain K_{vi} remains unchanged, the bandwidth increases as the proportional gain K_{vp} increases. The other parameters are same. Table II provides the parameters of the dc voltage controllers. The parameters of the current controller is same as those in Table I.

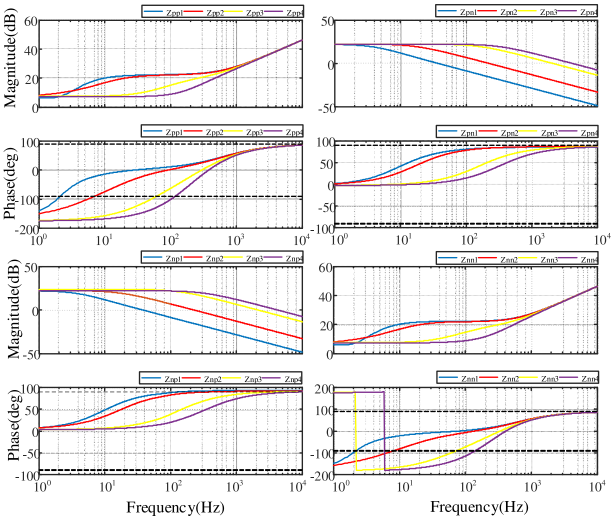

Fig. 11. Modeled impedance with different bandwidths.

In Fig. 11, the blue, red, yellow, and purple lines correspond with the impedance with different bandwidths 16, 75, 310, and 445 Hz, respectively. The four elements of the mirror-frequency impedance matrix are all plotted on the frequency range from 1 to 10^4 Hz. The black dotted line indicates that the phase is 90° or $-90°$. When the phase is more than 90° or less than $-90°$, there arises a negative impedance. It can be concluded from Fig. 11 that, as the bandwidth increases, the frequency range of the negative impedance expands. It can be seen that the frequency range of the negative impedance Z_{pp4} is from 1 to 100 Hz. The frequency range of the negative impedance Z_{pp1} is from 1 Hz to several hertz. Similarly, the impedance Z_{nn4} owns a wider frequency range of the negative impedance than Z_{nn3}, Z_{nn2}, and Z_{nn1}. The magnitudes of the positive and negative-mirror-frequency impedances Z_{pp} and Z_{nn} increase with the increase in frequency. The magnitudes of the cross-coupling impedance Z_{pn} and Z_{np} decrease with the increase in frequency. The bandwidth of the dc-link voltage control loop is wider, and the magnitudes of the cross-coupling impedance are larger. Besides, the magnitudes of the cross-coupling impedance are large enough and cannot be neglected. Therefore, the mirror-frequency impedance matrix cannot be diagonalized.

In summary, the wider bandwidth of the dc voltage controllers lead to a wider frequency range of the negative impedance and a higher magnitudes of the cross-coupling impedance. The negative impedance in the low frequency may cause the low-frequency oscillations [8], [9], [11]. The voltage source utilizes an ideal voltage source with no inner impedance, so the system is stable. The impedance-based stability will be analyzed in detail in future work.

B. Effects of DC-Link Voltage Ripple on Impedance Response

The dc-link capacitance plays a critical role in decreasing the dc-link voltage ripple. Four experiments with four sets of capacitance values $C_d = 50$ mF, $C_d = 9$ mF, $C_d = 6$ mF, and $C_d = 3$ mF are made in this section based on the HIL platform in Fig. 9. The ac-side voltages and currents and dc-side voltages of four experiments are shown on Fig. 12. Chart 0, Chart 2, Chart

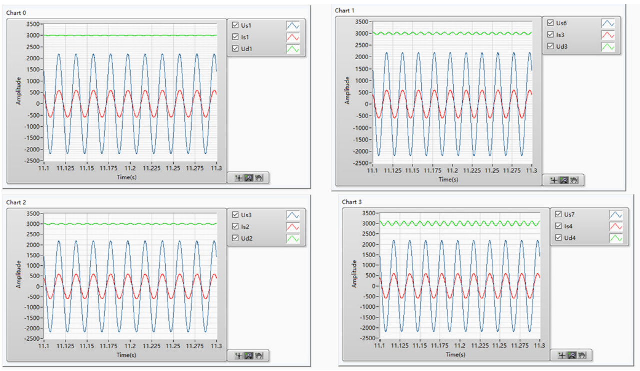

Fig. 12. AC voltages and currents and dc voltages of four experiments.

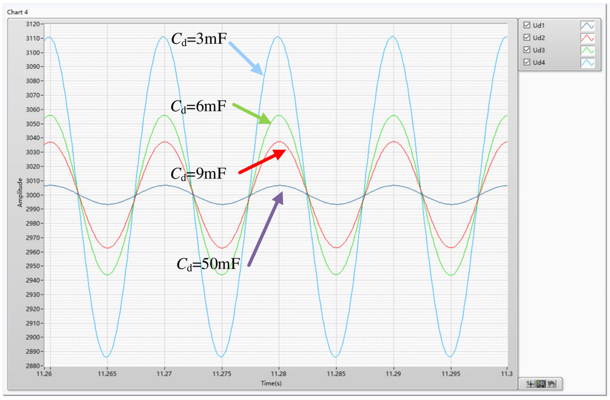

Fig. 13. DC voltage ripple.

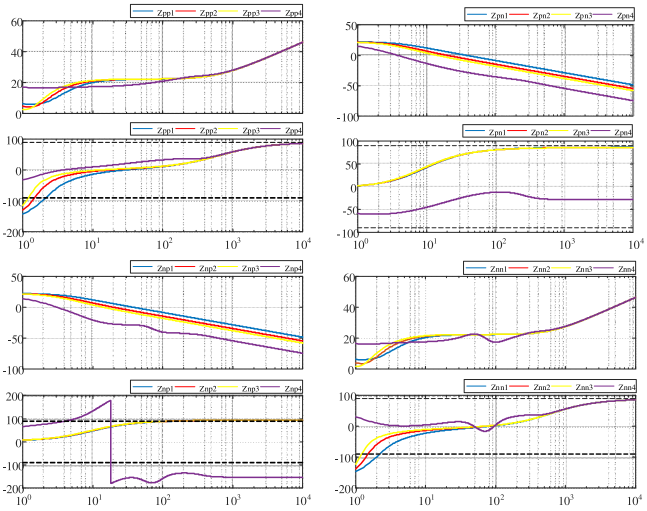

Fig. 14. Modeled impedance with different capacitances.

1, and Chart 3 correspond to $C_d = 50$ mF, $C_d = 9$ mF, $C_d = 6$ mF, and $C_d = 3$ mf, respectively. The dc-link voltage ripples of the four experiments are all plotted in Fig. 13.

It can be observed in Fig. 14 that the larger is the dc-link capacitance, the less is the amplitude of the dc-link voltage ripple. The modeled impedance with the four sets of capacitance are plotted on four sub-Bode diagrams in Fig. 14. The blue, red, yellow, and purple lines correspond with $C_d = 3$ mF, $C_d = 6$ mF, $C_d = 9$ mF, and $C_d = 50$ mF, respectively. It can be observed that the frequency ranges of negative impedance Z_{pp} sorted from the largest to the smallest are $Z_{pp1}, Z_{pp2}, Z_{pp3}$, and Z_{pp4}. And the frequency ranges of negative impedance Z_{nn} sorted from the largest to the smallest are $Z_{nn1}, Z_{nn2}, Z_{nn3}$, and Z_{nn4}. It can be concluded that a large dc-link capacitance can help decrease the frequency range of negative impedance and stabilize the system. The magnitude of Z_{pn1} is higher than Z_{pn2}, Z_{pn3}, and Z_{pn4}. And the magnitude of Z_{np1} is higher than Z_{np2}, Z_{np3}, and Z_{np4}. As the capacitance decreases, the magnitudes of the cross-coupling impedance increase.

VI. CONCLUSION

This paper focuses on the impedance modeling of single-phase converter systems in the stationary frame, with consideration of the voltage control loop, SOGI-PLL, and mirror-frequency effects. The simulations on the HIL verify the accuracy of the model and the measurement. Some conclusions are drawn as follows:

1) The mirror-frequency impedance modeling method based on harmonic linearization is valid and accurate for single-phase converter systems considering the voltage control loop and SOGI-PLL
2) The mirror-frequency impedance matrix of the single-phase systems is nondiagonal. The coupling elements are the same order magnitude as the diagonal ones. The single-phase system is a MIMO system. The mirror-frequency model can capture the cross-coupling dynamics.
3) The dc-link voltage control loop and ripples can change the impedance and cannot be neglected in impedance modeling. The wider bandwidth of the dc-link voltage control loop or the less dc-link capacitance can cause the wider frequency range of the negative impedance. The bandwidth of the dc-link voltage control loop is larger or the dc-link capacitance is less, the magnitudes of the cross-coupling impedance are larger.

APPENDIX

Substituting (18)–(20) into (22), the modulation signal $M[f]$ at frequency $f_p + f_1$ is deduced as

$$\begin{aligned} M_{\text{case4}}[f_p+f_1] &= V_d'\dot{V}_p^+ + V_d' K_{ip}\dot{I}_p^+ + V_d'\dot{V}_p^+(-j\omega_1 L_s \\ &\quad - R_s - K_{ip}) I_{\text{ref}} T_{\text{PLL}}(s)[H_\alpha(s+j\omega_1) + jH_\beta(s+j\omega_1)]/4 \\ &\quad + V_d'\dot{V}_p^+(j\omega_1 L_s - R_s - K_{ip}) I_{\text{ref}} T_{\text{PLL}}(s+j4\pi f_1) \\ &\quad \times [H_\alpha(s+j\omega_1) - jH_\beta(s+j\omega_1)]/4 \\ &\quad + V_d'\dot{V}_n^+(-j\omega_1 L_s - R_s - K_{ip}) I_{\text{ref}} T_{\text{PLL}}(s) \\ &\quad \times [H_\alpha(s-j\omega_1) - jH_\beta(s-j\omega_1)]/4 + 0.5 V_d' H_v[f_p] \\ &\quad \times [(1+j\cos\theta_{v1})\omega_1 L_s + (\cos\theta_{v1} - j)(K_{ip}+R_s)]\dot{V}_{dp}^+. \end{aligned} \tag{42}$$

Assuming

$$\begin{aligned} A_3 &= V_d'(-j\omega_1 L_s - R_s - K_{ip}) I_{\text{ref}} T_{\text{PLL}}(s)[H_\alpha(s+j\omega_1) \\ &\quad + jH_\beta(s+j\omega_1)]/4 + V_d'(j\omega_1 L_s - R_s - K_{ip}) I_{\text{ref}} T_{\text{PLL}} \\ &\quad \times (s+j4\pi f_1)[H_\alpha(s+j\omega_1) - jH_\beta(s+j\omega_1)]/4 \end{aligned} \tag{43}$$

$$\begin{aligned} A_4 &= V_d'(-j\omega_1 L_s - R_s - K_{ip}) I_{\text{ref}} T_{\text{PLL}}(s)[H_\alpha(s-j\omega_1) \\ &\quad - jH_\beta(s-j\omega_1)]/4 \end{aligned} \tag{44}$$

$$Z_{pp\_\mathrm{case4}} = \frac{R_s + j2\pi(f_p + f_1)L_s + V_d' V_d K_{ip} + (V_d B_1 + \dot{M}_1^+)/G(\dot{I}_1^- V_d' K_{ip} + \dot{M}_1^-)}{1 - V_d' V_d - V_d A_3 - (V_d B_1 + \dot{M}_1^+)/G(\dot{I}_1^- V_d' + \dot{I}_1^- A_3 + \dot{I}_1^+ A_5)} \tag{56}$$

$$Z_{pn\_\mathrm{case4}} = \frac{(V_d B_1 + \dot{M}_1^+)/G(\dot{I}_1^+ V_d' K_{ip} + \dot{M}_1^+)}{1 - V_d' V_d - V_d A_3 - (V_d B_1 + \dot{M}_1^+)/G(\dot{I}_1^- V_d' + \dot{I}_1^- A_3 + \dot{I}_1^+ A_5)} \tag{57}$$

$$Z_{np\_\mathrm{case4}} = \frac{(B_2 V_d + \dot{M}_1^-)/G(\dot{I}_1^- V_d' K_{ip} + \dot{M}_1^-)}{1 - V_d' V_d - V_d A_6 - (B_2 V_d + \dot{M}_1^-)/G(\dot{I}_1^+ V_d' + \dot{I}_1^- A_4 + \dot{I}_1^+ A_6)} \tag{59}$$

$$Z_{nn\_\mathrm{case4}} = \frac{R_s + j2\pi(f_p - f_1)L_s + V_d' V_d K_{ip} + (B_2 V_d + \dot{M}_1^-)/G(\dot{I}_1^+ V_d' K_{ip} + \dot{M}_1^+)}{1 - V_d' V_d - V_d A_6 - (B_2 V_d + \dot{M}_1^-)/G(\dot{I}_1^+ V_d' + \dot{I}_1^- A_4 + \dot{I}_1^+ A_6)} \tag{60}$$

$$\begin{aligned} B_1 = {} & 0.5V_d' H_v[f_p][(1 + j\cos\theta_{v1})\omega_1 L_s \\ & + (\cos\theta_{v1} - j)(K_{ip} + R_s)]. \end{aligned} \tag{45}$$

Equation (42) can be rewritten as

$$\begin{aligned} M_{\mathrm{case4}}[f_p + f_1] = {} & V_d' \dot{V}_p^+ + V_d' K_{ip} \dot{I}_p^+ + A_3 \dot{V}_p^+ + A_4 \dot{V}_n^+ \\ & + B_1 \dot{V}_{dp}^+. \end{aligned} \tag{46}$$

Substituting (18)–(20) into (22), the modulation signal $M[f]$ at frequency $f_p - f_1$ is deduced as

$$\begin{aligned} M_{\mathrm{case4}}[f_p - f_1] = {} & V_d' \dot{V}_n^+ + V_d' K_{ip} \dot{I}_n^+ + V_d' \dot{V}_p^+ (j\omega_1 L_s \\ & - R_s - K_{ip}) I_{\mathrm{ref}} T_{\mathrm{PLL}}(s)[H_\alpha(s + j\omega_1) + jH_\beta(s + j\omega_1)]/4 \\ & + V_d' \dot{V}_n^+ (j\omega_1 L_s - R_s - K_{ip}) I_{\mathrm{ref}} T_{\mathrm{PLL}}(s)[H_\alpha(s - j\omega_1) \\ & - jH_\beta(s - j\omega_1)]/4 + V_d' \dot{V}_n^+ (-j\omega_1 L_s - R_s - K_{ip}) I_{\mathrm{ref}} T_{\mathrm{PLL}} \\ & \times (s - j4\pi f_1)[H_\alpha(s - j\omega_1) + jH_\beta(s - j\omega_1)]/4 \; 0.5V_d' H_{vp} \\ & \times [(1 - j\cos\theta_{v1})\omega_1 L_s + (\cos\theta_{v1} + j)(K_{ip} + R_s)]\dot{V}_{dp}^+. \end{aligned} \tag{47}$$

Assuming

$$\begin{aligned} A_5 = {} & V_d'(j\omega_1 L_s - R_s - K_{ip}) I_{\mathrm{ref}} T_{\mathrm{PLL}}(s)[H_\alpha(s + j\omega_1) \\ & + jH_\beta(s + j\omega_1)]/4 \end{aligned} \tag{48}$$

$$\begin{aligned} A_6 = {} & V_d'(j\omega_1 L_s - R_s - K_{ip}) I_{\mathrm{ref}} T_{\mathrm{PLL}}(s)[H_\alpha(s - j\omega_1) \\ & - jH_\beta(s - j\omega_1)]/4 + V_d'(-j\omega_1 L_s - R_s - K_{ip}) I_{\mathrm{ref}} T_{\mathrm{PLL}} \\ & \times (s - j4\pi f_1)[H_\alpha(s - j\omega_1) + jH_\beta(s - j\omega_1)]/4 \end{aligned} \tag{49}$$

$$\begin{aligned} B_2 = {} & 0.5V_d' H_{vp}[(1 - j\cos\theta_{v1})\omega_1 L_s \\ & + (\cos\theta_{v1} + j)(K_{ip} + R_s)]. \end{aligned} \tag{50}$$

Equation (47) can be rewritten as

$$\begin{aligned} M_{\mathrm{case4}}[f_p - f_1] = {} & V_d' \dot{V}_n^+ + V_d' K_{ip} \dot{I}_n^+ \\ & + A_5 \dot{V}_p^+ + A_6 \dot{V}_n^+ + B_2 \dot{V}_{dp}^+. \end{aligned} \tag{51}$$

Substituting (43) and (48) into (25), (25) is rewritten as

$$\begin{aligned} (1/R_d + j2\pi f_p C_d)\dot{V}_{dp}^+ = {} & \dot{I}_1^- (V_d' \dot{V}_p^+ + V_d' K_{ip} \dot{I}_p^+ + A_3 \dot{V}_p^+ \\ & + A_4 \dot{V}_n^+ + B_1 \dot{V}_{dp}^+) + \dot{I}_1^+ (V_d' \dot{V}_n^+ + V_d' K_{ip} \dot{I}_n^+ + A_5 \dot{V}_p^+ \\ & + A_6 \dot{V}_n^+ + B_2 \dot{V}_{dp}^+) + \dot{M}_1^+ \dot{I}_n^+ + \dot{M}_1^- \dot{I}_p^+. \end{aligned} \tag{52}$$

Solving (52), it can be rewritten as

$$\begin{aligned} (1/R_d + j2\pi f_p C_d - \dot{I}_1^- B_1 - \dot{I}_1^+ B_2)\dot{V}_{dp}^+ = {} & \dot{V}_p^+ (\dot{I}_1^- V_d' \\ & + \dot{I}_1^- A_3 + \dot{I}_1^+ A_5) + \dot{V}_n^+ (I_1^+ V_d' + \dot{I}_1^- A_4 + \dot{I}_1^+ A_6) \\ & + \dot{I}_p^+ (\dot{I}_1^- V_d' K_{ip} + \dot{M}_1^-) + \dot{I}_n^+ (\dot{I}_1^+ V_d' K_{ip} + \dot{M}_1^+). \end{aligned} \tag{53}$$

Assuming

$$G = (1/R_d + j2\pi f_p C_d - \dot{I}_1^- B_1 - \dot{I}_1^+ B_2). \tag{54}$$

Substituting (46), (53), and (54) into (24), the frequency-domain equation at frequency $f_p + f_1$ can be rewritten as

$$\begin{aligned} \dot{V}_p^+ - [R_s + j2\pi(f_p + f_1)L_s]\dot{I}_p^+ = {} & V_d' V_d \dot{V}_p^+ + V_d' V_d K_{ip} \dot{I}_p^+ \\ & + V_d A_3 \dot{V}_p^+ + (V_d B_1 + \dot{M}_1^+)/G(\dot{I}_1^- V_d' + \dot{I}_1^- A_3 \\ & + \dot{I}_1^+ A_5)\dot{V}_p^+ + (V_d B_1 + \dot{M}_1^+)/G(\dot{I}_1^- V_d' K_{ip} + \dot{M}_1^-)\dot{I}_p^+ \\ & + (V_d B_1 + M_1^+)/G(\dot{I}_1^+ V_d' K_{ip} + \dot{M}_1^+)\dot{I}_n^+. \end{aligned} \tag{55}$$

Solving (53), the closed-loop mirror-frequency impedance Z_{pp} and Z_{pn} are deduced as (56) and (57) as shown at the top of the page.

Substituting (46), (53), and (54) into (24), the frequency-domain equation at frequency $f_p - f_1$ can be rewritten as

$$\begin{aligned} & \dot{V}_n^+ - [R_s + j2\pi(f_p - f_1)L_s]\dot{I}_n^+ \\ & = V_d' V_d \dot{V}_n^+ + V_d' V_d K_{ip} \dot{I}_n^+ + V_d A_6 \dot{V}_n^+ \\ & \quad + (B_2 V_d + \dot{M}_1^-)/G(\dot{I}_1^+ V_d' + \dot{I}_1^- A_4 + \dot{I}_1^+ A_6)\dot{V}_n^+ \\ & \quad + (B_2 V_d + \dot{M}_1^-)/G(\dot{I}_1^- V_d' K_{ip} + \dot{M}_1^-)\dot{I}_p^+ \\ & \quad + (B_2 V_d + \dot{M}_1^-)/G(\dot{I}_1^+ V_d' K_{ip} + \dot{M}_1^+)\dot{I}_n^+. \end{aligned} \tag{58}$$

Solving (58), the closed-loop mirror-frequency impedance Z_{np} and Z_{nn} are deduced as (59) and (60) as shown at the top of the page.

REFERENCES

[1] X. Wang, F. Blaabjerg, and W. Wu, "Modeling and analysis of harmonic stability in an AC power-electronics-based power system," *IEEE Trans. Power Electron.*, vol. 29, no. 12, pp. 6421–6432, Dec. 2014, doi: 10.1109/TPEL.2014.2306432.

[2] J. B. Kwon, X. Wang, F. Blaabjerg, C. L. Bak, A. R. Wood, and N. R. Watson, "Harmonic instability analysis of a single-phase grid-connected converter using a harmonic state-space modeling method," *IEEE Trans. Ind. Appl.*, vol. 52, no. 5, pp. 4188–4200, Sep./Oct. 2016, doi: 10.1109/TIA.2016.2581154.

[3] M. Cespedes and J. Sun, "Impedance modeling and analysis of grid-connected voltage-source converters," *IEEE Trans. Power Electron.*, vol. 29, no. 3, pp. 1254–1261, Mar. 2014, doi: 10.1109/TPEL.2013.2262473.

[4] X. Wang, L. Harnefors, and F. Blaabjerg, "Unified impedance model of grid-connected voltage-source converters," *IEEE Trans. Power Electron.*, vol. 33, no. 2, pp. 1775–1787, Feb. 2018, doi: 10.1109/TPEL.2017.2684906.

[5] Y. Wang, X. Wang, F. Blaabjerg, and Z. Chen, "Harmonic instability assessment using state-space modeling and participation analysis in inverter-fed power systems," *IEEE Trans. Ind. Electron.*, vol. 64, no. 1, pp. 806–816, Jan. 2017, doi: 10.1109/TIE.2016.2588458.

[6] Z. Liu, G. Zhang, and Y. Liao, "Stability research of high-speed railway EMUs and traction network cascade system considering impedance matching," *IEEE Trans. Ind. Appl.*, vol. 52, no. 5, pp. 4315–4326, Sep./Oct. 2016, doi: 10.1109/TIA.2016.2574770.

[7] Y. Liao, Z. Liu, G. Zhang, and C. Xiang, "Vehicle-Grid system modeling and stability analysis with forbidden region-based criterion," *IEEE Trans. Power Electron.*, vol. 32, no. 5, pp. 3499–3512, May 2017, doi: 10.1109/TPEL.2016.2587726.

[8] Y. Liao, Z. Liu, H. Zhang, and B. Wen, "Low-Frequency stability analysis of single-phase system with dq-frame impedance approach—Part I: Impedance modeling and verification," *IEEE Trans. Ind. Appl.*, vol. 54, no. 5, pp. 4999–5011, Sep./Oct. 2018, doi: 10.1109/TIA.2018.2832027.

[9] Y. Liao, Z. Liu, H. Zhang, and B. Wen, "Low-Frequency stability analysis of single-phase system with dq-frame impedance approach—Part II: Stability and frequency analysis," *IEEE Trans. Ind. Appl.*, vol. 54, no. 5, pp. 5012–5024, Sep./Oct. 2018, doi: 10.1109/TIA.2018.2828386.

[10] H. Wang, W. Mingli, and J. Sun, "Analysis of low-frequency oscillation in electric railways based on small-signal modeling of vehicle-grid system in dq frame," *IEEE Trans. Power Electron.*, vol. 30, no. 9, pp. 5318–5330, Sep. 2015, doi: 10.1109/TPEL.2015.2388796.

[11] H. Hu, H. Tao, F. Blaabjerg, X. Wang, Z. He, and S. Gao, "Train–Network interactions and stability evaluation in high-speed railways—Part I: Phenomena and modeling," *IEEE Trans. Power Electron.*, vol. 33, no. 6, pp. 4627–4642, Jun. 2018, doi: 10.1109/TPEL.2017.278188.

[12] J. Sun, "Small-Signal methods for AC distributed power systems—A review," *IEEE Trans. Power Electron.*, vol. 24, no. 11, pp. 2545–2554, Nov. 2009, doi: 10.1109/TPEL.2009.2029859.

[13] M. Belkhayat, "Stability criteria for AC power systems with regulated loads," Ph.D. dissertation, Purdue Univ., West Lafayette, IN, Dec. 1997.

[14] J. Huang, K. A. Corzine, and M. Belkhayat, "Small-Signal impedance measurement of power-electronics-based AC power systems using line-to-line current injection," *IEEE Trans. Power Electron.*, vol. 24, no. 2, pp. 445–455, Feb. 2009, doi: 10.1109/TPEL.2008.2007212.

[15] A. Rygg, M. Molinas, C. Zhang, and X. Cai, "A modified sequence-domain impedance definition and its equivalence to the dq-domain impedance definition for the stability analysis of AC power electronic systems," *IEEE J. Emerg. Sel. Top. Power Electron.*, vol. 4, no. 4, pp. 1383–1396, Dec. 2016, doi: 10.1109/JESTPE.2016.2588733.

[16] M. K. Bakhshizadeh *et al.*, "Couplings in phase domain impedance modeling of grid-connected converters," *IEEE Trans. Power Electron.*, vol. 31, no. 10, pp. 6792–6796, Oct. 2016, doi: 10.1109/TPEL.2016.2542244.

[17] C. Zhang, X. Cai, A. Rygg, and M. Molinas, "Sequence domain SISO equivalent models of a grid-tied voltage source converter system for small-signal stability analysis," *IEEE Trans. Energy Convers.*, vol. 33, no. 2, pp. 741–749, Jun. 2018, doi: 10.1109/TEC.2017.2766217.

[18] S. Shah and L. Parsa, "On impedance modeling of single-phase voltage source converters," in *Proc. IEEE Energy Convers. Congr. Expo.*, Milwaukee, WI, USA, 2016, pp. 1–8, doi: 10.1109/ECCE.2016.7855302.

[19] D. Lu, X. Wang, and F. Blaabjerg, "Impedance-based analysis of DC-link voltage dynamics in voltage-source converters," *IEEE Trans. Power Electron.*, doi: 10.1109/TPEL.2018.2856745.

[20] J. Sun and H. Liu, "Impedance modeling and analysis of modular multilevel converters," in *Proc. IEEE 17th Workshop Control Model. Power Electron.*, Trondheim, 2016, pp. 1–9, doi: 10.1109/COMPEL.2016.7556781.

[21] B. Wen, D. Boroyevich, R. Burgos, P. Mattavelli, and Z. Shen, "Small-Signal stability analysis of three-phase AC systems in the presence of constant power loads based on measured d-q frame impedances," *IEEE Trans. Power Electron.*, vol. 30, no. 10, pp. 5952–5963, Oct. 2015, doi: 10.1109/TPEL.2014.2378731.

[22] S. Lissandron, L. Dalla Santa, P. Mattavelli, and B. Wen, "Experimental validation for impedance-based small-signal stability analysis of single-phase interconnected power systems with grid-feeding inverters," *IEEE J. Emerg. Sel. Top. Power Electron.*, vol. 4, no. 1, pp. 103–115, Mar. 2016, doi: 10.1109/JESTPE.2015.2477902.

[23] C. Zhang, X. Wang, and F. Blaabjerg, "Analysis of phase-locked loop influence on the stability of single-phase grid-connected inverter," in *Proc. IEEE 6th Int. Symp. Power Electron. Distrib. Gener. Syst.*, Aachen, Germany, 2015, pp. 1–8, doi: 10.1109/PEDG.2015.7223089.

[24] J. Sun and H. Liu, "Sequence impedance modeling of modular multilevel converters," *IEEE J. Emerg. Sel. Top. Power Electron.*, vol. 5, no. 4, pp. 1427–1443, Dec. 2017, doi: 10.1109/JESTPE.2017.2762408.

[25] S. Shah and L. Parsa, "Small-signal modeling of single-phase PLLs using harmonic signal-flow graphs," in *Proc. IEEE Energy Convers. Congr. Expo.*, Cincinnati, OH, USA, 2017, pp. 4989–4995, doi: 10.1109/ECCE.2017.8096844.

[26] J. Sun, Z. Bing, and K. J. Karimi, "Input impedance modeling of multipulse rectifiers by harmonic linearization," *IEEE Trans. Power Electron.*, vol. 24, no. 12, pp. 2812–2820, Dec. 2009, doi: 10.1109/TPEL.2009.2033067.

[27] M. Chen and J. Sun, "Low-frequency input impedance modeling of boost single-phase PFC converters," *IEEE Trans. Power Electron.*, vol. 22, no. 4, pp. 1402–1409, Jul. 2007, doi: 10.1109/TPEL.2007.900592.

[28] G. Francis, R. Burgos, D. Boroyevich, F. Wang, and K. Karimi, "An algorithm and implementation system for measuring impedance in the D-Q domain," in *Proc. IEEE Energy Convers. Congr. Expo.*, Phoenix, AZ, USA, 2011, pp. 3221–3228, doi: 10.1109/ECCE.2011.6064203.

[29] K. Wang, X. Huang, B. Fan, Q. Yang, G. Li, and M. L. Crow, "Decentralized power sharing control for parallel-connected inverters in islanded single-phase micro-grids," *IEEE Trans. Smart Grid*, doi: 10.1109/TSG.2017.2720683.

Han Zhang (S'18) received the B. S. degree in electrical engineering and its automation in 2017 from Southwest Jiaotong University, Chengdu, China, where he is currently working toward the M.S. degree in electrical engineering.

His current research interests include impedance modeling and stability analysis of single-phase source voltage converters based on harmonic linearization.

Zhigang Liu (M'06–SM'16) received the Ph.D. degree in power system and automation from Southwest Jiaotong University, Chengdu, China, in 2003.

He is currently a Full Professor with the School of Electrical Engineering, Southwest Jiaotong University. His current research interests include electrical relationship of vehicle-grid in high-speed railways, power quality considering grid-connect of new energies, pantograph-catenary dynamics, fault detection, status assessment, and active control.

Dr. Liu was elected as a fellow of The Institution of Engineering and Technology (IET) in 2017. He is an Associate Editor of the IEEE Transactions on Instrumentation and Measurement and IEEE Access. He is also an Editorial Board Member of the IEEE Transactions on Vehicular Technology.

Siqi Wu (S'18) received the B.S. degree in electrical engineering and its automation from Huaqiao University, Xiamen, China, in 2016. She is currently working toward the Ph.D. degree at the School of Electrical Engineering, Southwest Jiaotong University, Chengdu, China.

Her research interests include the modeling and stability analysis of power electronics-based systems.

Zhiyuan Li received the B.S. degree in electrical engineering and its automation in 2017 from Southwest Jiaotong University, Chengdu, China, where he is currently working toward the master's degree at the School of Electrical Engineering.

His current research interests include the application of MMC-STATCOM and CHB-STATCOM in high-speed railways.